RADIATION PATTERNS OF COMPRESSIONAL AND SHEAR TRANSDUCERS AT THE SURFACE OF AN ELASTIC HALF SPACE

by

X.M. Tang

NER Geoscience
1100 Crown Colony Drive
Quincy, MA 02169

Zhenya Zhu, and M.N. Toksöz

Earth Resources Laboratory
Department of Earth, Atmospheric, and Planetary Sciences
Massachusetts Institute of Technology
Cambridge, MA 02139

ABSTRACT

The radiation patterns of an elastic wave field generated by circular plane compressional and shear transducers are derived using the method of steepest descent. These patterns contain both effects of the elastic half space and the amplitude modulation due to the finite dimension of the piston source. Behaviors of radiation patterns of the generated compressional and shear waves are shown for low, medium, and high frequencies. Laboratory experiments have been performed to measure radiation patterns of compressional and shear transducers. Theory and experiment are found to be in good agreement.

INTRODUCTION

In measurements with solid seismic models or in the non-destructive testing of solid materials, circular transducer sources are usually applied at the surface of the solid to generate wave signals. The directivity or radiation pattern of the sources is important for the understanding of the behavior of the generated wave field. For materials without shear modulus (acoustic media), the directivity function is well known, as given by $[2J_1(k_ca\sin\theta)/k_ca\sin\theta)]$ (e.g., Gooberman, 1969), where k_c is the acoustic wavenumber, a is the piston radius, θ is the polar angle measured from the piston axis, and J_1 is the ordinary Bessel function of order one. Because this directivity is well established and widely used, it tends to be over-generalized to describe the radiation pattern in an

elastic medium without noticing the effects due to the solid surface and the coupling between the generated compressional and shear waves. In this study, we will address the problem and present complete expressions for the radiation patterns of a piston source in an elastic medium.

The radiation due to surface point forces into an elastic half space was first treated by Lamb (1904). A review of the "Lamb's problem" and its theoretical development were given by Ewing et al. (1957). Miller and Pursey (1954) studied the radiation of a vertical point source; Cherry (1962) studied the radiation of a horizontal point source. Johnson (1974) presented the complete solution of Green's function for the elastic half space. In these studies, the forces acting on the surface of the half space were idealized as point forces, partly because these studies were aimed at geophysical applications, where the dimension of the source is often negligible. However, in applications with piston sources of finite size, the source dimension plays an important role in determining the radiation of the wave field. Tang et al. (1990) have recently studied the radiation of piston sources into an elastic half space. By using Johnson's (1974) Green's function, they derived integral expressions of the elastic displacements for both compressional and shear piston sources acting on the surface of an elastic half space. But in that study the primary concern was the diffraction effects in the axial direction of the source. In the present study, the integral expressions of Tang et al. (1990) will be employed to obtain radiation patterns for both compressional and shear piston sources. The theoretical results will also be verified with a laboratory experimental study.

THEORETICAL DEVELOPMENT

Let us consider the configuration of Figure 1, where a circular compressional or shear piston source of radius a is applied at the surface of an elastic half space. We will use two coordinate systems. One is Cartesian system $\{x, y, z\}$; the other is spherical system $\{R, \theta, \phi\}$, as indicated in Figure 1. The solutions of elastic displacements in Tang et al. (1990) are given in Cartesian coordinates, which will be transformed into spherical coordinates to obtain radiation patterns.

Assuming that the stress (compressional or shear) over the piston surface is uniformly distributed, Tang et al. (1990) derived the generated elastic displacements $\vec{u}(u_x, u_y, u_z)$ in the half space, which are given as:

for the compressional source (stress σ_{zz} acting in z–direction),

$$u_x = -\frac{a\sigma_{zz}(\omega)\cos\phi}{2\pi\mu} \int_0^\infty \left[\frac{2k^2 - k_\beta^2}{F(k)} e^{-\nu z} - \frac{2\nu\nu'}{F(k)} e^{-\nu' z} \right] J_1(ka) J_1(kr) k\,dk$$

$$u_y = -\frac{a\sigma_{zz}(\omega)\sin\phi}{2\pi\mu} \int_0^\infty \left[\frac{2k^2 - k_\beta^2}{F(k)} e^{-\nu z} - \frac{2\nu\nu'}{F(k)} e^{-\nu' z} \right] J_1(ka) J_1(kr) k\,dk$$

$$u_z = -\frac{a\sigma_{zz}(\omega)}{2\pi\mu} \int_0^\infty \left[\frac{2k^2 - k_\beta^2}{F(k)} \nu e^{-\nu z} - \frac{2k^2\nu}{F(k)} e^{-\nu' z} \right] J_1(ka) J_0(kr) dk \tag{1}$$

for the shear source (stress σ_{xz} acting in x–direction),

$$
\begin{aligned}
u_x &= \frac{a\sigma_{xz}(\omega)}{4\pi\mu} \int_0^\infty \left[-\frac{2k^2\nu'}{F(k)} e^{-\nu z} \right. \\
&\quad + \left. \frac{(3k^2 - 2k_\beta^2)(2k^2 - k_\beta^2) - 4\nu\nu' k^2}{\nu' F(k)} e^{-\nu' z} \right] J_1(ka) J_0(kr) dk \\
&\quad + \frac{a\sigma_{13}(\omega)\cos 2\phi}{4\pi\mu} \int_0^\infty \left[\frac{2k^2\nu'}{F(k)} e^{-\nu z} + \frac{(2k^2 - k_\beta^2) - 4\nu\nu'}{\nu' F(k)} k^2 e^{-\nu' z} \right] J_1(ka) J_2(kr) dk \\
u_y &= \frac{a\sigma_{xz}(\omega)\sin 2\phi}{4\pi\mu} \int_0^\infty \left[\frac{2k^2\nu'}{F(k)} e^{-\nu z} + \frac{(2k^2 - k_\beta^2) - 4\nu\nu'}{\nu' F(k)} k^2 e^{-\nu' z} \right] J_1(ka) J_2(kr) dk \\
u_z &= \frac{a\sigma_{xz}(\omega)\cos\phi}{2\pi\mu} \int_0^\infty \left[\frac{2\nu\nu'}{F(k)} e^{-\nu z} - \frac{2k^2 - k_\beta^2}{F(k)} e^{-\nu' z} \right] J_1(ka) J_1(kr) k\, dk \tag{2}
\end{aligned}
$$

where

$$
\begin{aligned}
r &= R\sin\theta \ , & z &= R\cos\theta \ , \\
k_\alpha &= \omega/\alpha \ , & k_\beta &= \omega/\beta \ , \\
\nu &= \sqrt{k^2 - k_\alpha^2} \ , & \nu' &= \sqrt{k^2 - k_\beta^2} \ , \\
F(k) &= (2k^2 - k_\beta^2)^2 - 4\nu\nu' k^2 \ , &&
\end{aligned}
$$

ω is angular frequency, α and β are compressional and shear velocities, respectively, and λ and μ are elastic constants. In the spherical coordinates, the displacement components (u_R, u_θ, u_ϕ) are related to the Cartesian components (u_x, u_y, u_z) through the following transformations:

$$
\begin{aligned}
u_R &= u_x \cos\phi \sin\theta + u_y \sin\phi \sin\theta + u_z \cos\theta \\
u_\theta &= u_x \cos\phi \cos\theta + u_y \sin\phi \cos\theta - u_z \sin\theta \\
u_\phi &= -u_x \sin\phi + u_y \cos\phi .
\end{aligned} \tag{3}
$$

We now proceed to derive the far-field expressions of the displacements (Eqs. (1) and (2)) using the method of steepest descent. To illustrate the application of the method and validity of the result, we consider the simple case of radiation of a piston source into an acoustic medium. Given a uniform displacement u_0 over the piston surface, the displacement potential φ in the medium is expressed by the King integral (Harris, 1982)

$$\varphi = au_0 \int_0^\infty \frac{\exp(-\sqrt{k^2 - k_c^2}\, z)}{\sqrt{k^2 - k_c^2}} J_0(kr) J_1(ka) dk \ , \tag{4}$$

where k_c is acoustic wavenumber. Using the identities for Bessel and Hankel functions

$$J_n(kr) = [H_n^{(1)}(kr) + H_n^{(2)}(kr)]/2 \ \text{ and } \ H_n^{(1)}(-kr) = (-1)^{n+1} H_n^{(2)}(kr) \ ,$$

and the expression of Hankel function at large kr,

$$H_n^{(2)}(kr) \sim \sqrt{\frac{2}{\pi kr}} \exp[-i(kr - n\pi/2 - \pi/2)] \quad ,$$

we can write Eq. (4) as

$$\varphi = \int_{-\infty}^{+\infty} G(k) \exp[\psi(k)] dk \quad , \tag{5}$$

where $G(k) = au_0 J_1(ka)(2/\pi kr)^{1/2}/(k^2 - k_c^2)^{1/2}$ and $\psi(k) = -i[(k^2 - k_c^2)^{1/2}z + kr - \pi/4]$. The steepest descent solution of Eq. (5) is (Aki and Richards, 1980)

$$\varphi = \sqrt{2\pi} G(k_0) \frac{\exp\left\{\psi(k_0) + i\arg[\psi''(k_0)]\right\}}{\sqrt{|\psi''(k_0)|}} \quad , \tag{6}$$

where $k_0 = k_c \sin\theta$ and $\psi''(k_0) = iz/(k_c \cos^3\theta)$. This results in the far-field solution for φ:

$$\varphi = \frac{u_0 a^2}{2} \frac{\exp(-ik_c R)}{R} \left[\frac{2J_1(k_c a \sin\theta)}{k_c a \sin\theta}\right] \quad . \tag{7}$$

The term in the square bracket is the previously mentioned directivity function of acoustic radiation. Since this result can also be derived using other techniques (e.g., Gooberman, 1969), the validity of the steepest descent result is thus verified. Returning to the elastic problem, we apply the method of steepest descent to the integral expressions in Eqs. (1) and (2). The far-field results of u_x, u_y, and u_z are then substituted into Eq. (3) to obtain the displacement components in the spherical coordinates. Omitting the lengthy algebra, we present the results in the following:

for the compressional source,

$$
\begin{aligned}
u_R &= \frac{a^2 \sigma_{zz}}{4\pi\mu} \frac{\exp(-ik_\alpha R)}{R} \left[\frac{2J_1(k_\alpha a \sin\theta)}{k_\alpha a \sin\theta}\right] \\
&\times \frac{(\beta/\alpha)^2 \cos\theta[1 - 2(\beta/\alpha)^2 \sin^2\theta]}{[1 - 2(\beta/\alpha)^2 \sin^2\theta]^2 + 4(\beta/\alpha)^3 \sin^2\theta \cos\theta[1 - (\beta/\alpha)^2 \sin^2\theta]^{1/2}} \quad , \tag{8}
\end{aligned}
$$

$$
\begin{aligned}
u_\theta &= -\frac{a^2 \sigma_{zz}}{2\pi\mu} \frac{\exp(-ik_\beta R)}{R} \left[\frac{2J_1(k_\beta a \sin\theta)}{k_\beta a \sin\theta}\right] \\
&\times \frac{\sin\theta \cos\theta[(\beta/\alpha)^2 - \sin^2\theta]^{1/2}}{(1 - 2\sin^2\theta)^2 + 4\sin^2\theta \cos\theta[(\beta/\alpha)^2 - \sin^2\theta]^{1/2}} \quad , \tag{9}
\end{aligned}
$$

$$u_\phi = 0 \quad , \tag{10}$$

for the shear source,

$$u_R = \frac{a^2 \sigma_{xz}}{2\pi\mu} \frac{\exp(-ik_\alpha R)}{R} \left[\frac{2J_1(k_\alpha a \sin\theta)}{k_\alpha a \sin\theta}\right]$$

$$\times \quad \frac{(\beta/\alpha)^3 \cos\phi \sin\theta \cos\theta [1 - 2(\beta/\alpha)^2 \sin^2\theta]^{1/2}}{[1 - 2(\beta/\alpha)^2 \sin^2\theta]^2 + 4(\beta/\alpha)^3 \sin^2\theta \cos\theta [1 - (\beta/\alpha)\sin^2\theta]^{1/2}} \quad , \quad (11)$$

$$u_\theta \quad = \quad \frac{a^2 \sigma_{xz}}{4\pi\mu} \frac{\exp(-ik_\beta R)}{R} \left[\frac{2J_1(k_\beta a \sin\theta)}{k_\beta a \sin\theta} \right]$$

$$\times \quad \frac{\cos\phi \cos\theta (1 - 2\sin^2\theta)}{(1 - 2\sin^2\theta)^2 + 4\sin^2\theta \cos\theta [(\beta/\alpha)^2 - \sin^2\theta]^{1/2}} \quad , \quad (12)$$

$$u_\phi \quad = \quad -\frac{a^2 \sigma_{xz}}{4\pi\mu} \frac{\exp(-ik_\beta R)}{R} \left[\frac{2J_1(k_\beta a \sin\theta)}{k_\beta a \sin\theta} \right] \sin\phi \quad . \quad (13)$$

The results presented in Eqs. (8) through (13) show that the far-field wave signals radiated by a shear or compressional piston separate into individual compressional and shear waves in the R, θ, and ϕ directions, as indicated by the propagation factors $\exp(-ik_\alpha R)$ and $\exp(-ik_\beta R)$, although these waves are intimately coupled in the near-field of the piston source (Tang et al., 1990). The dependence of wave amplitude on angles θ and ϕ depicts the radiation patterns of the compressional or shear piston. For the compressional piston, symmetry around z—axis makes u_ϕ zero and u_R and u_θ independent of ϕ. For the shear piston, symmetry about z—axis does not exist, and the displacements u_R, u_θ, and u_ϕ are dependent on ϕ.

The angular dependence of the displacements in Eqs. (8) through (13) can be separated into two parts. The first is the function in the square brackets of these equations. This function has the same functional form as the directivity function for acoustic media (Eq. (7)), and represents the modulation of a finite size piston on the radiated wave field. The modulation for compressional and shear waves are different, as can be seen from the different wavenumbers appearing in the modulation function. In addition, this function is strongly dependent on the operating frequency of the piston source. The second is the remaining part in the angular dependent terms. This part is entirely independent of frequency and represents the effects of an elastic half space on the radiation of a point compressional or shear force. In fact, if we let the transducer surface shrink to a point ($a \to 0$) and keep the quantity $0.5a^2\sigma_{zz}$ (or σ_{xz}) constant, the piston modulation functions then approach 1. Eqs. (8) through (10) reduce identically to the results of Miller and Pursey (1954) for a compressional point source, and Eqs. (11) through (13) reduce to the results of Cherry (1962) for a shear point source. By these comparisons, it is clear that the effect of a finite size piston (shear or compressional) is the modulation of the radiated compressional and shear waves by a directivity function $[2J_1(k_\gamma a \sin\theta)/k_\gamma a \sin\theta]$, where $k_\gamma = k_\alpha$ for compressional waves and $k_\gamma = k_\beta$ for shear waves. Because a single shear or compressional piston can generate both compressional and shear waves, two such directivity functions are needed to characterize the elastic radiation of the piston. Whereas in an acoustic medium, one directivity function suffices to describe the radiation pattern.

THEORETICAL EXAMPLES

To show the radiation patterns of compressional and shear transducers, we numerically evaluated Eqs. (8) through (12). In the calculation, we used a transducer radius of 0.7 cm. The compressional and shear velocities of the elastic medium were assumed to be 6400 km/s and 3100 m/s, respectively. The calculated results are scaled by $a\sigma_{zz}$ (or $\sigma_{zz})/(4\pi\mu R)$. Amplitudes of the calculated u_R and u_θ are then taken and are plotted versus angle θ as polar plots. For the compressional source, the results depend on θ only. For the shear source, we present the results in the plane that contains the source polarization direction (i.e., ϕ=0). For the u_ϕ component of the shear source, the dependence on θ is the same as the acoustic case. Thus the radiation pattern of u_ϕ will not be shown here. In the following, the radiation patterns will be shown for three different (low, medium, and high) frequencies. They are 0.1 MHz, 0.5 MHz, and 1 MHz, respectively.

Figure 2 shows the radiation pattern of the u_R component due to the compressional source. For the 0.1 MHz case, the wavelength is much larger than the source dimension, so that the radiation pattern resembles that of a point compressional source (White, 1983). As frequency increases, the modulation due to transducer dimension becomes important. At 1 MHz, a directed radiation pattern is formed, which is very similar to that of the acoustic case. Figure 3 shows the shear component u_θ generated by the compressional source. Because the radiated amplitudes of u_θ at low and high frequencies are different by an order of magnitude, we plot the 0.1 MHz result separately in Figure 3a, which again is very similar to the result of a point source (White, 1983). With increasing frequency, the radiation pattern becomes complicated. At 1 MHz, the pattern shows several lobes (Figure 3b).

Figure 4 shows the radiation patterns of the u_θ component due to the shear source (a=0.7 cm) for the three frequencies. For the 0.1 MHz case, the pattern is also similar to the point source result, the drastic change of amplitude at the angle $\theta = \sin^{-1}(\beta/\alpha)$ being due to the phase shift occurring at this angle. (See Eq. (12), and also Figure 3a and Eq. (8)). The 0.5 and 1 MHz results show that the pattern becomes directed towards the axial direction, similar to the case of acoustic radiation. For the compressional wave generated by the shear source (Figure 5), the radiated amplitude is much smaller than the shear amplitude, as can be seen by comparing the amplitude scales of Figures 4 and 5. At 1 MHz, the radiated P-wave amplitude is small and the pattern shows the presence of multiple lobes (Figure 5).

COMPARISON WITH LABORATORY RESULTS

Experimental Procedure

In order to test the validity of the radiation patterns given by Eqs. (8) through (13), we carried out laboratory experiments to measure the radiation pattern of compressional (denoted by P) and shear (denoted by S) transducers as a function of θ. The laboratory model was an aluminum half cylinder of 30.48 cm in diameter and 15.24 cm in height. The compressional and shear velocities of the model are $\alpha= 6400$ m/s and $\beta= 3100$ m/s, respectively. Its density is 2.7 kg/m^3. The P transducer has a radius of 0.635 cm and the S transducer 1.27 cm. The receiver is a transducer with compressional (denoted by P) and shear (denoted by S) piezoelectrical disks stacked together. The radius of the transducer is 0.79 cm. The transmitting and receiving configurations with the model are illustrated in Figure 6.

For the P transducer, its radiated radial (u_R) and transverse (u_θ) components were respectively measured using the receiver transducer with P and S disks. The P disk measures u_R, while the S disk, with its polarization pointing to the increasing (or decreasing) θ direction, measures the u_θ component of the wave field. For the S transducer, the same receiver was used to receive the radiated radial (u_R) and transverse (u_θ) components in the $\phi = 0$ plane. It is noted that the radiation patterns given by Eqs. (8) through (13) are calculated only for a single frequency (e.g., Figures 2 through 5). Thus the radiation pattern should also be measured around the frequency. Experimentally, this can be done by measuring both amplitude and the center frequency of the received P and S waves (note that the waves may have very different frequency content because the P and S components of the receiver have different frequency responses). For the P and S sources and the 2-component receiver, the center frequencies of four transmitting-receiving pairs are: 860 kHz for the P transmitting and P receiving (denoted by P-P) pair, 300 kHz for the P-S pair, 430 kHz for the S-S pair, and 800 kHz for the S-P pair. For these frequencies and the transducer dimensions, the waves received at the circumference of the model (30.48 cm away from the source) are clearly in the far-field of the source. Therefore, the radiation patterns can be calculated for these frequencies using the given properties of the model and the transducer dimensions. The experimental radiation patterns can be obtained by directly measuring the wave amplitudes at various θ angles. The theoretical and experimental patterns can then be compared. Because the coupling effects between the transducer and aluminum model are difficult to estimate, we do not show the absolute amplitudes of the measured radiation patterns. Instead, these patterns are properly scaled to fit the corresponding theoretical patterns. In addition, because of the symmetry of the patterns about θ, we only measured the wave amplitudes for $0 < \theta < 90^o$.

Experimental Results

Figure 7 shows the comparison of the theory (solid curves) with experiment (solid circles) for the P-P transmitting and receiving pair (i.e., u_R in Eq. (8)). As seen from this figure, theory and experiment are in excellent agreement. The radiation shows a strongly directed pattern at the frequency of 860 kHz. Figure 8 shows the comparison for the P-S pair (i.e., u_θ in Eq. (9)). The theory (solid curves) and experiment (solid circles) are also in very good agreement. Both theory and experiment show that the radiation pattern is pointed away from the axial direction of the transducer and has two lobes in the (first) quadrant. Of particular interest are the radiation patterns of the S transducer. Although an analogy with the acoustic case may seem inappropriate because a shear vibration cannot generate wave motion in an acoustic medium, certain similarity does exist for the S-S transmitting and receiving pair. Figure 9 shows the predicted and measured radiation patterns at 430 kHz for the S-S pair. Again, we found excellent agreement between theory and experiment. Because of the much larger transducer radius and slower velocity ($\beta < \alpha$) compared to the P-P case (Figure 7), the S source radiation pattern is even more strongly directed towards the axial direction, even though the frequency (430 kHz) is much lower than the P-P case (860 kHz). The radiation pattern is very similar to that of the acoustic radiation. For the u_R component received by the P disk of the receiver (S-P case), the radiation pattern shows somewhat complicated features (Figure 10). The theoretical pattern shows that there are three lobes in the radiation pattern in either the first or second quadrant. The lobe closest to the $\theta = 0$ direction has the largest amplitude, which is verified by the experiment. In addition, the lobe close to the $\theta = 90^o$ direction can also be observed from the measured data. However, the lobe in the middle cannot be seen clearly in the experiment. This discrepancy may be attributed to such effects as transducer-model coupling and the averaging of the received signal due to the finite dimension of the receiver. Despite this discrepancy, the theory and experiment are in fairly good agreement.

CONCLUSIONS

Through the analysis of far-field behavior of the wave field generated by compressional and shear transducers, we have obtained complete expressions for the radiation patterns of the transducers. Although these results are obtained assuming a constant stress distribution over the source surface, the results will still be valid if the actual stress is not constant over the source surface, because in the far-field the difference between the constant and non-constant stress distributions is not discernible. Comparison of the theoretical radiation patterns with those measured using actual transducers shows very good agreement between theory and experiment. Comparing the elastic radiation patterns with that of the acoustic case, we see that the u_R component of a compressional source and the u_θ component of a shear source have patterns similar to the acoustic

radiation pattern, with some modification due to the elastic half space. The u_θ component of a compressional source and the u_R component of a shear source have patterns that are pointed away from the axial direction of the source, but these patterns are strongly modulated by a directivity function similar to that of the acoustic case.

ACKNOWLEDGEMENTS

APPENDIX: WAVEFORMS FOR MEASURING RADIATION PATTERNS

In Figs. A1–A4, we show the laboratory experimental waveforms from which the radiation patterns were measured.

REFERENCES

Aki, K., and P. Richards, 1980, *Quantitative Seismology–Theory and Methods* (Freeman, San Francisco).

Cherry, J.T., Jr., 1962, "The azimuthal and polar radiation patterns obtained from a horizontal stress applied at the surface of an elastic half space," *Bull. Seismol. Soc. Am., 52,* 27–36.

Ewing, W.M., W.S. Jardetzky, and F. Press, 1957, *Elastic Waves in Layered Media,* McGraw-Hill, New York.

Gooberman, G.L., 1968, *Ultrasonics: Theory and Application,* Hart Publishing Company, New York.

Harris, G.R., 1981, "Review of transient field theory for a baffled planar piston," *J. Acoust. Soc. Am., 70,* 10–20.

Johnson, L.E, 1974, "Green's function for Lamb's problem," *Geophys. J. Roy. Astr. Soc., 37,* 99–131.

Miller, G.F., and H. Pursey, 1954, "The field and radiation impedance of mechanical radiators on the free surface of a semi-infinite isotropic solid," *Proc. R. Soc. London, Ser. A,* 223: 521–541.

Tang., X.M., M.N. Toksöz, and C.H. Cheng, 1990, "Elastic wave radiation and diffraction of a piston source," *J. Acoust. Soc. Am., 87,* 1894–1902.

White, J.E., 1983, *Underground Sound,* Elsevier, New York.
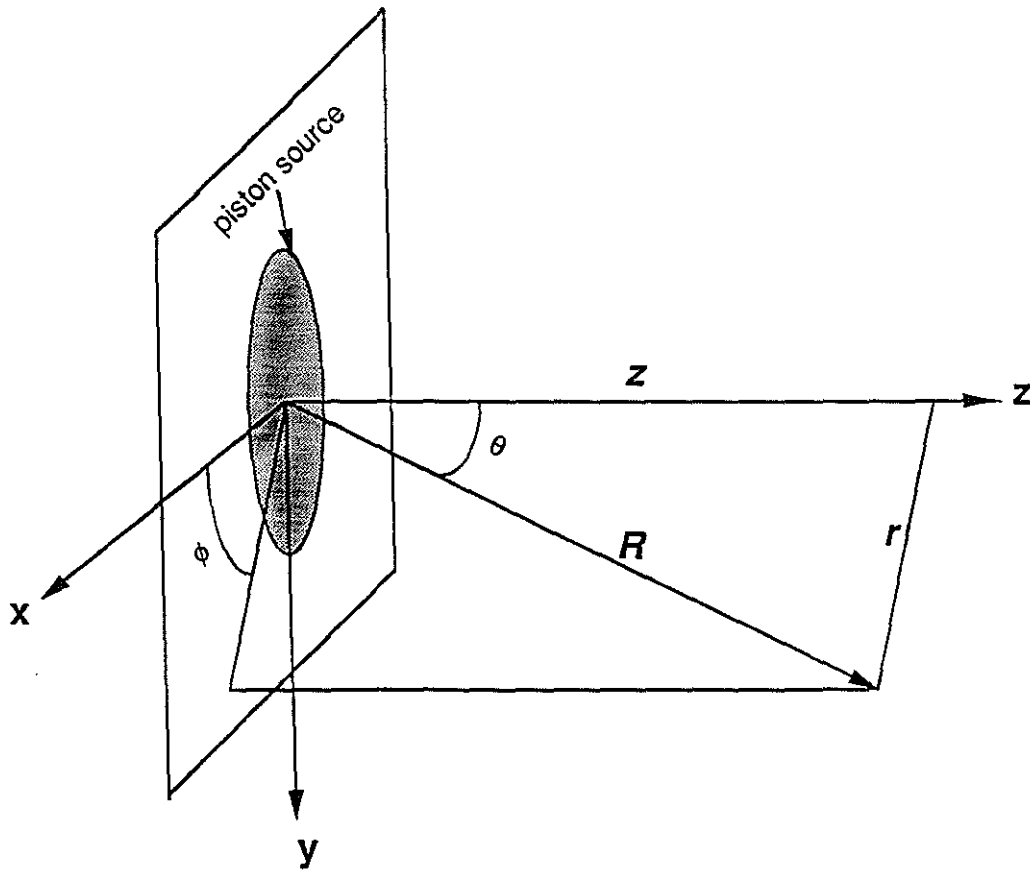
Figure 1: Diagram showing the transducer source at the surface of an elastic half space and the $\{x, y, z\}$ and $\{R, \theta, \phi\}$ coordinate systems.
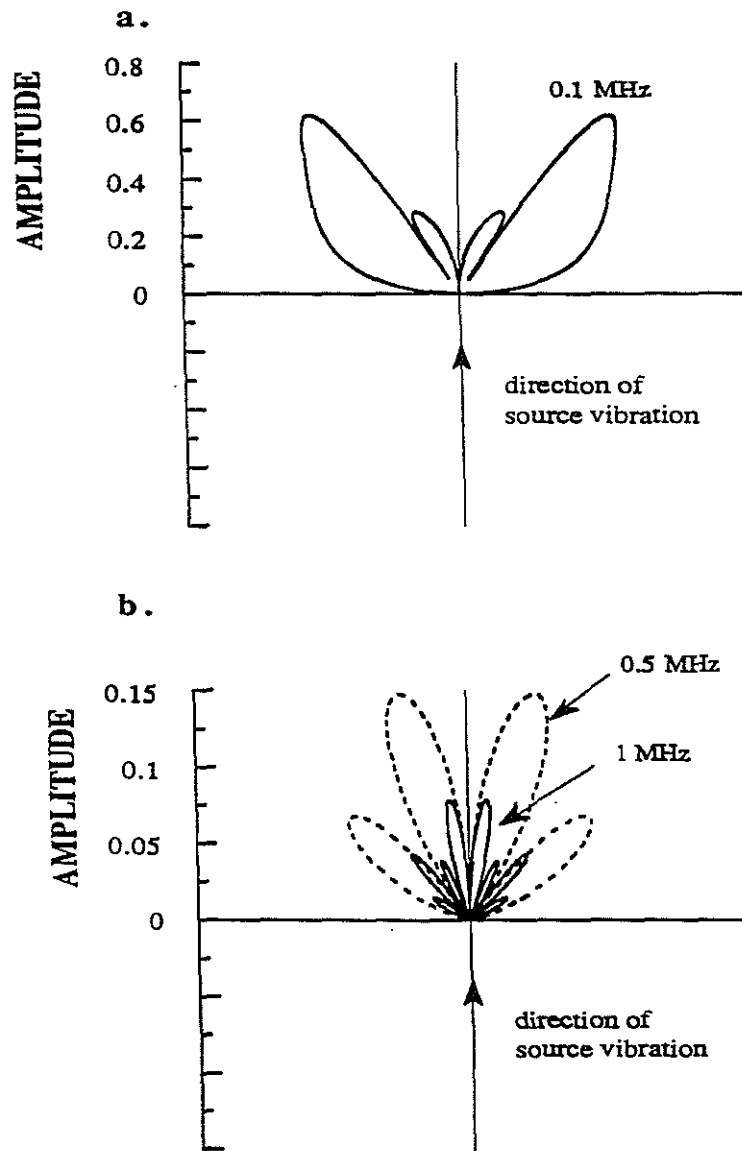
u$_R$ (compressional) due to compressional source
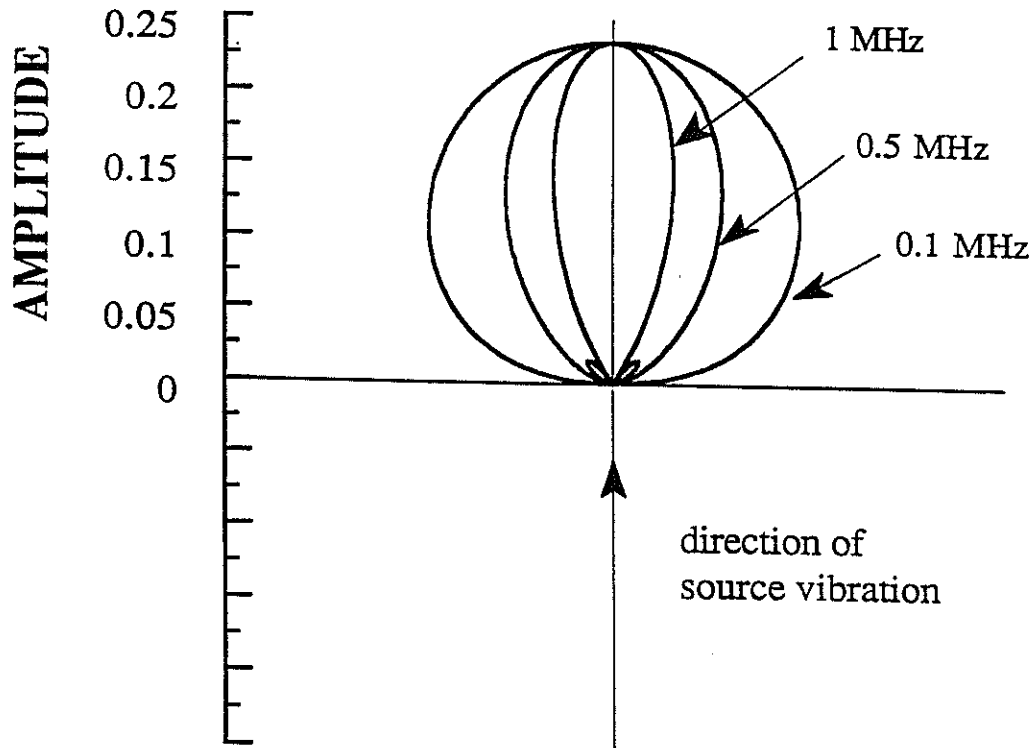
Figure 2: Radiation pattern for the u_R component of a compressional source (a =0.7 cm) at frequencies 0.1, 0.5, and 1 MHz. At 0.1 MHz, the pattern is close to that of a point source. With increasing frequency, the pattern becomes directed towards the axial direction, due to the modulation of the source dimension.

u$_\theta$ (shear) due to compressional source

a.

b.

Figure 3: Radiation pattern for the u_θ component of a compressional source (a =0.7 cm) at frequencies 0.1 MHz (a), 0.5 and 1 MHz (b).

Tang et al.

u$_\theta$ (shear) due to shear source
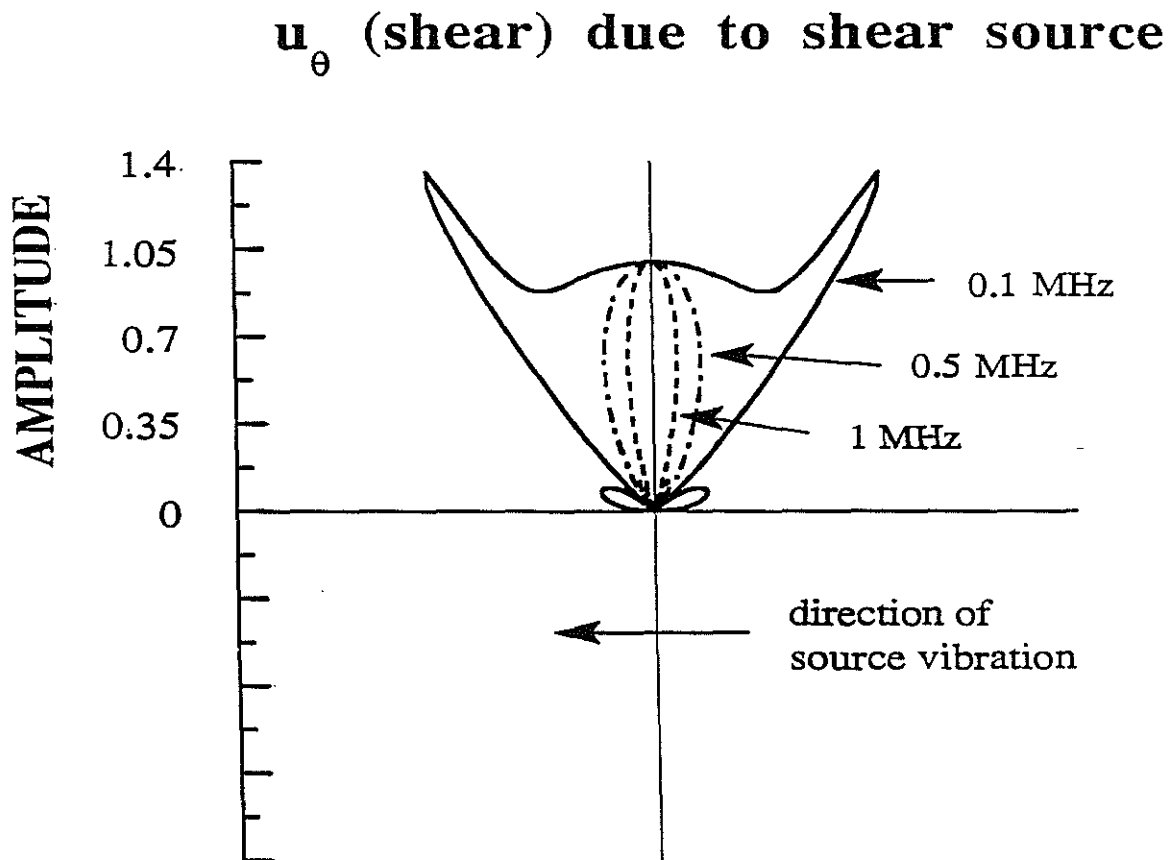
Figure 4: Radiation pattern for the u_θ component of a shear source (a =0.7 cm) at frequencies 0.1, 0.5, and 1 MHz.

u$_R$ (compressional) due to shear source
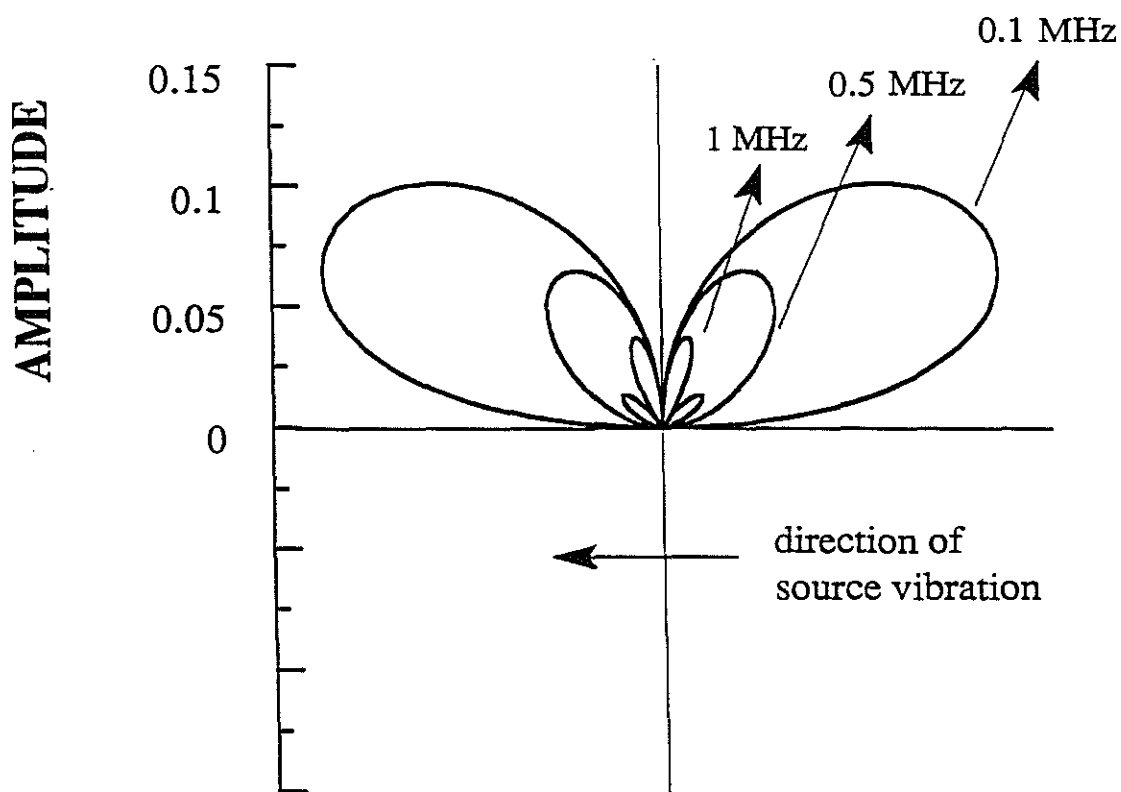
Figure 5: Radiation pattern for the u_R component of a shear source (a =0.7 cm) at frequencies 0.1, 0.5, and 1 MHz.

Source

Aluminum Model
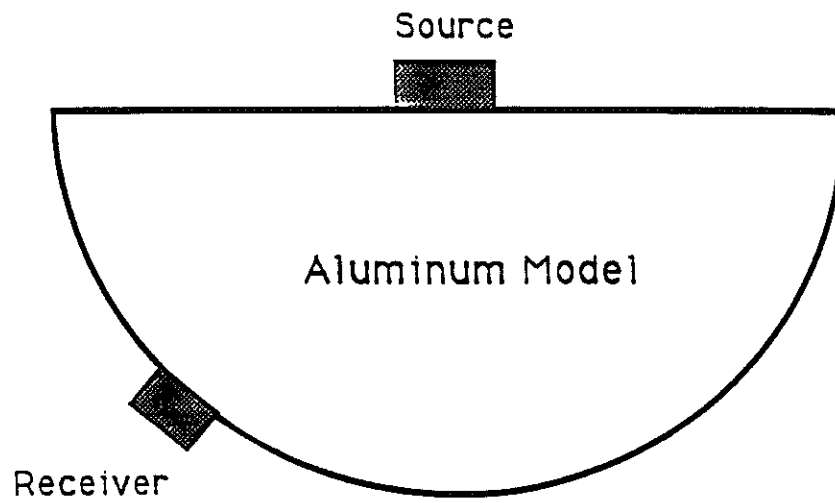
Receiver

Figure 6: Laboratory experimental setup for measuring radiation patterns of compressional and shear transducer sources. The radius of the model (or source-receiver distance) is 30.48 cm.
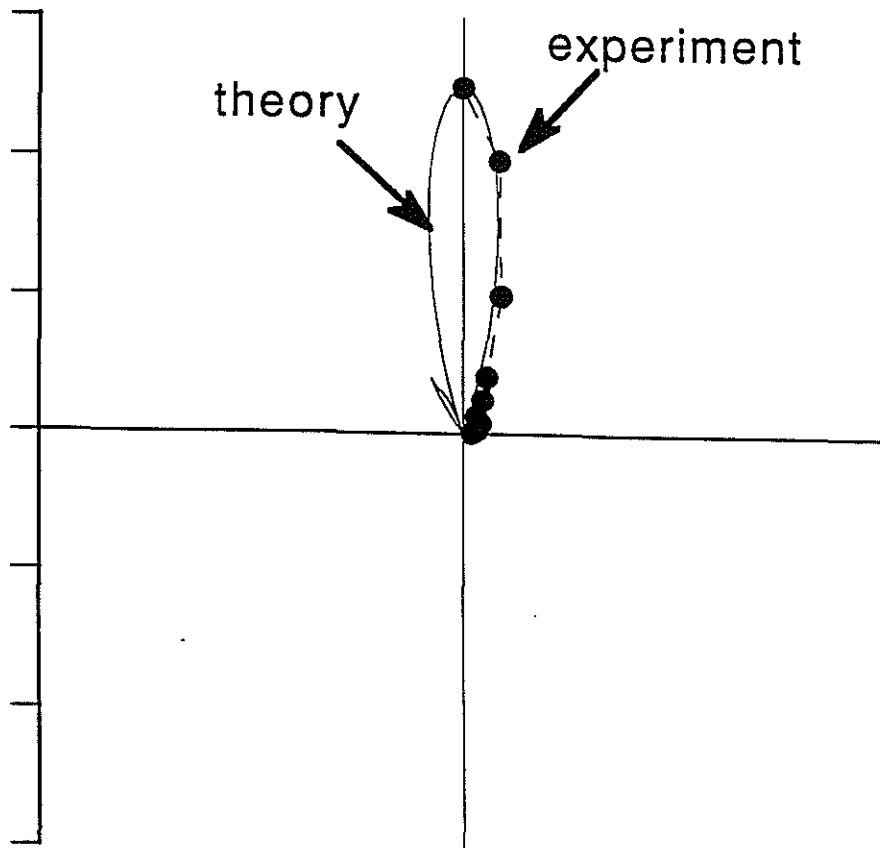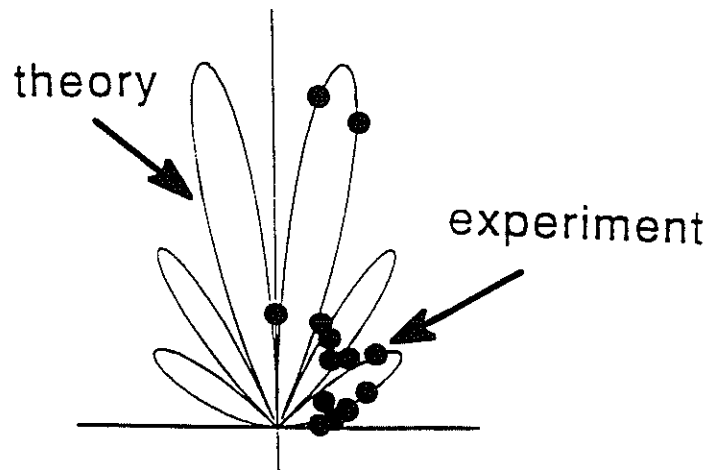
P source --- P receiver
(freq = 860 kHz)
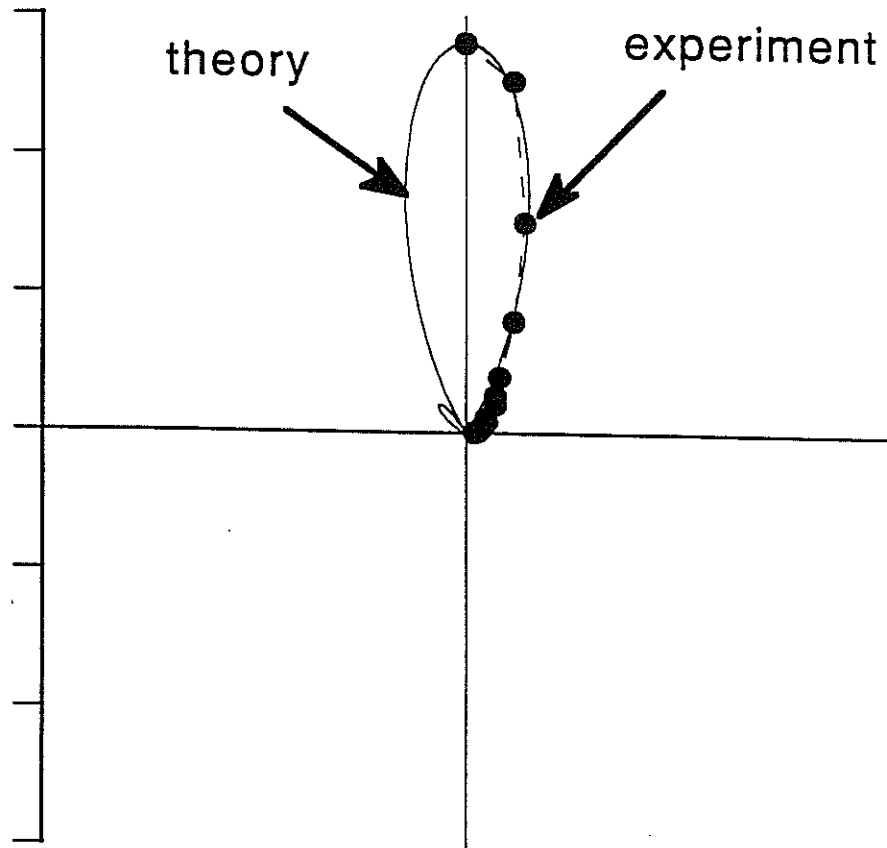
theory experiment

Figure 7: Comparison of theoretical (solid curve) and experimental (solid circles) radiation patterns for the u_R component of the compressional transducer ($a = 0.635$ cm) at 864 kHz.

P source --- S receiver
(freq= 300 kHz)
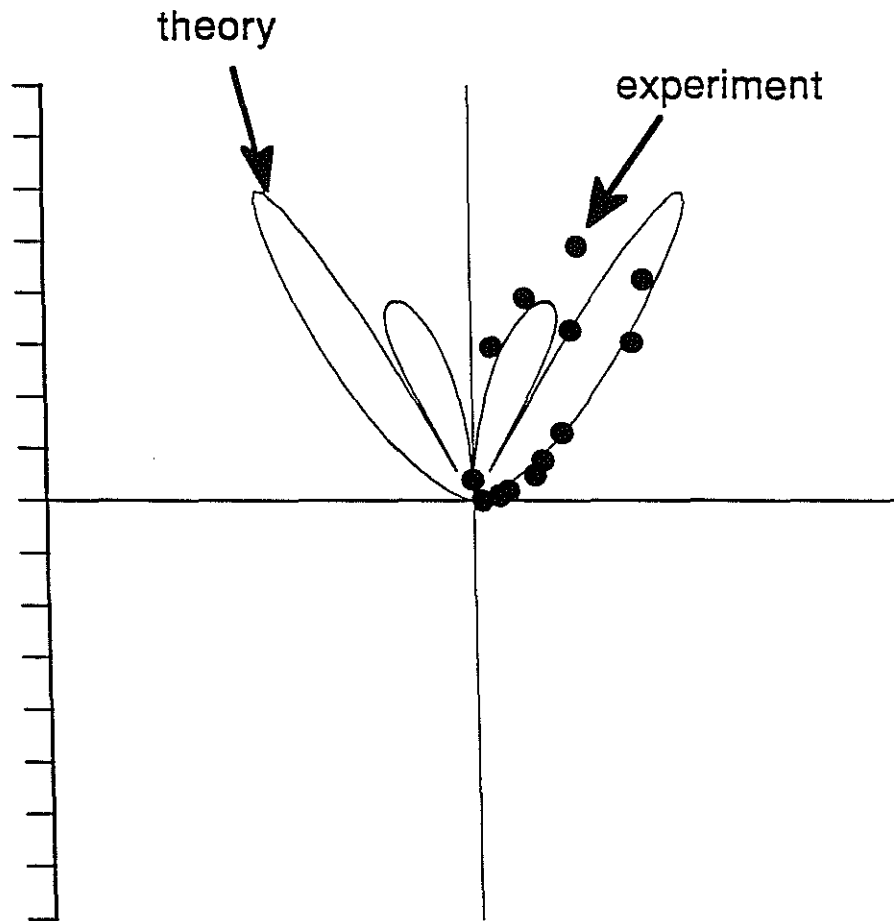
Figure 8: Comparison of theoretical (solid curve) and experimental (solid circles) radiation patterns for the u_θ component of the compressional transducer (a =0.635 cm) at 300 kHz.

Figure 9: Comparison of theoretical (solid curve) and experimental (solid circles) radiation patterns for the u_θ component of the shear transducer (a =1.27 cm) at 430 kHz.

S source --- P receiver
(freq = 800 kHz)

Figure 10: Comparison of theoretical (solid curve) and experimental (solid circles) radiation patterns for the u_R component of the shear transducer ($a =1.27$ cm) at 800 kHz.
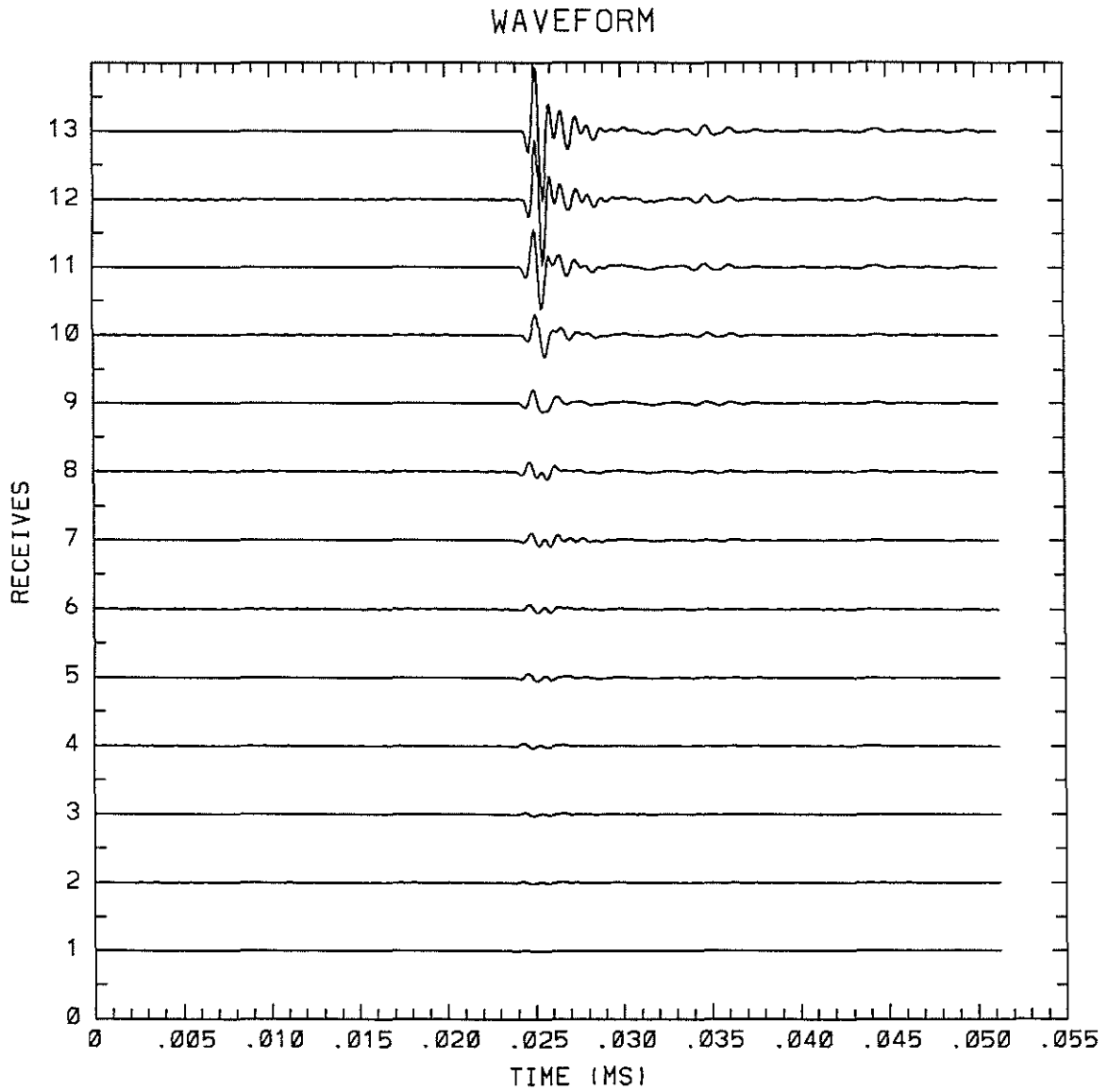
WAVEFORM

Figure A-1: Waveforms measured at various azimuthal directions from the source transducer (P source and P receiver).
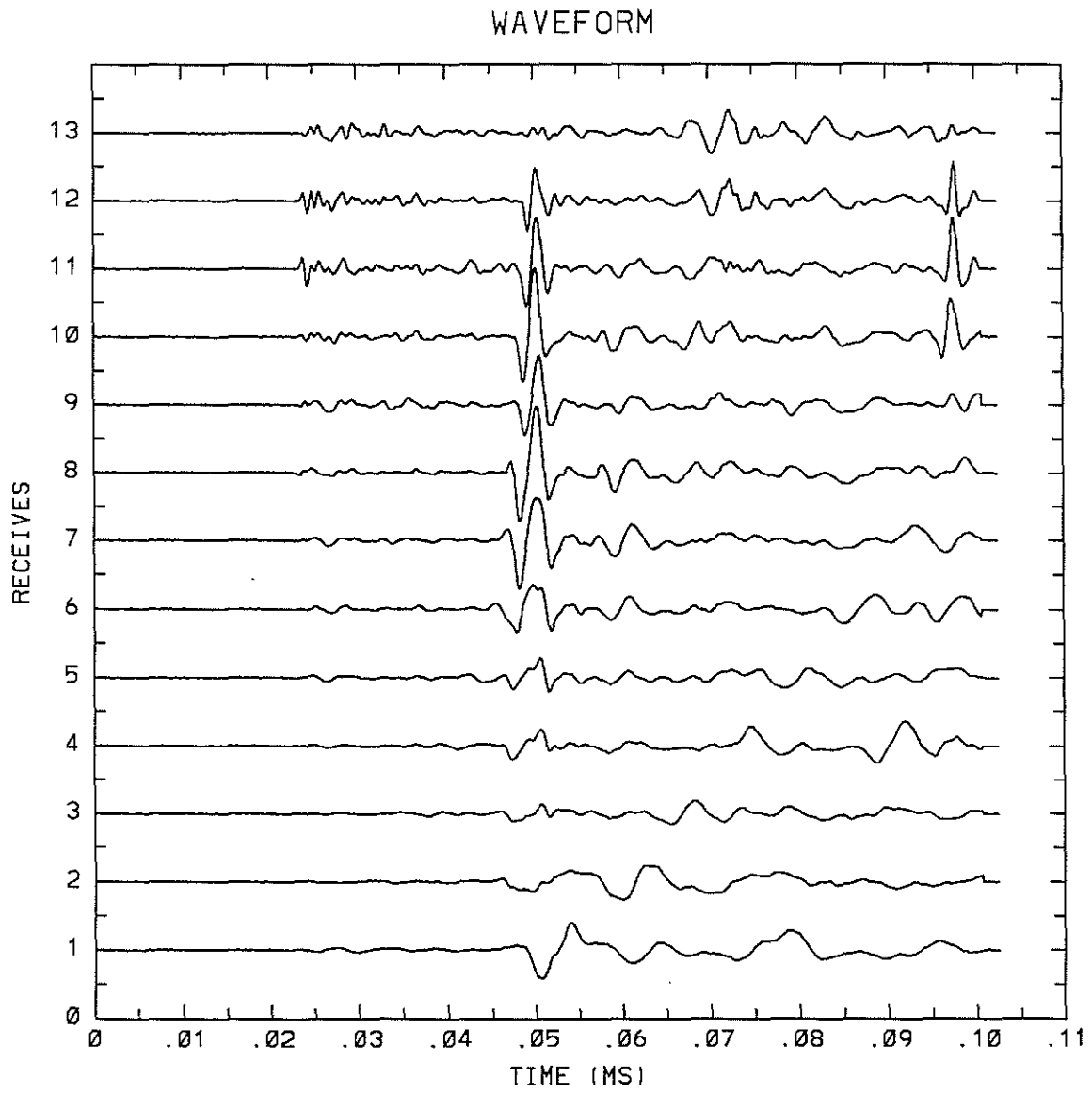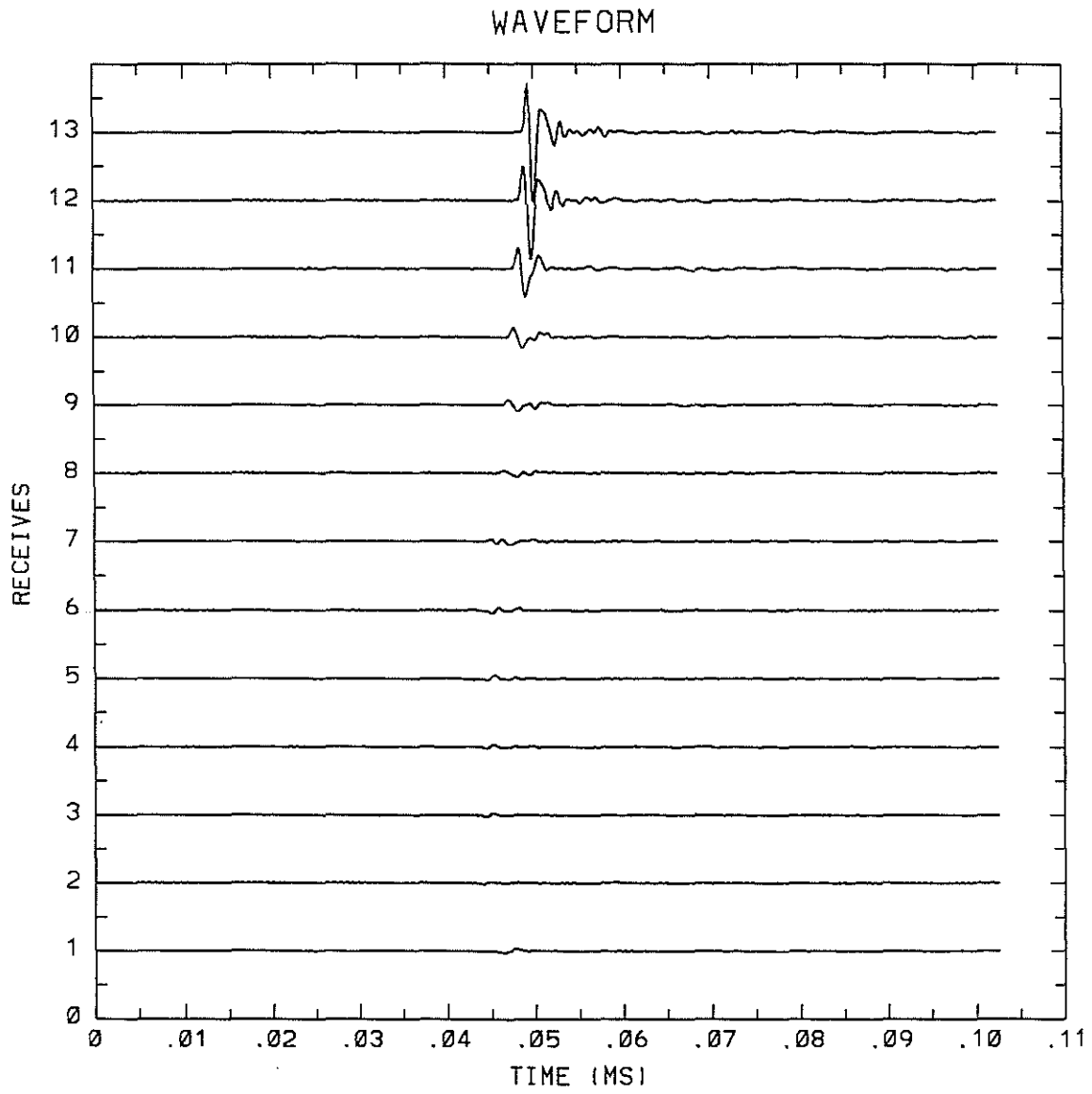
Tang et al.

WAVEFORM

Figure A-2: Waveforms measured at various azimuthal directions from the source transducer (P source and S receiver).

WAVEFORM

Figure A-3: Waveforms measured at various azimuthal directions from the source trans-
ducer (S source and S receiver).
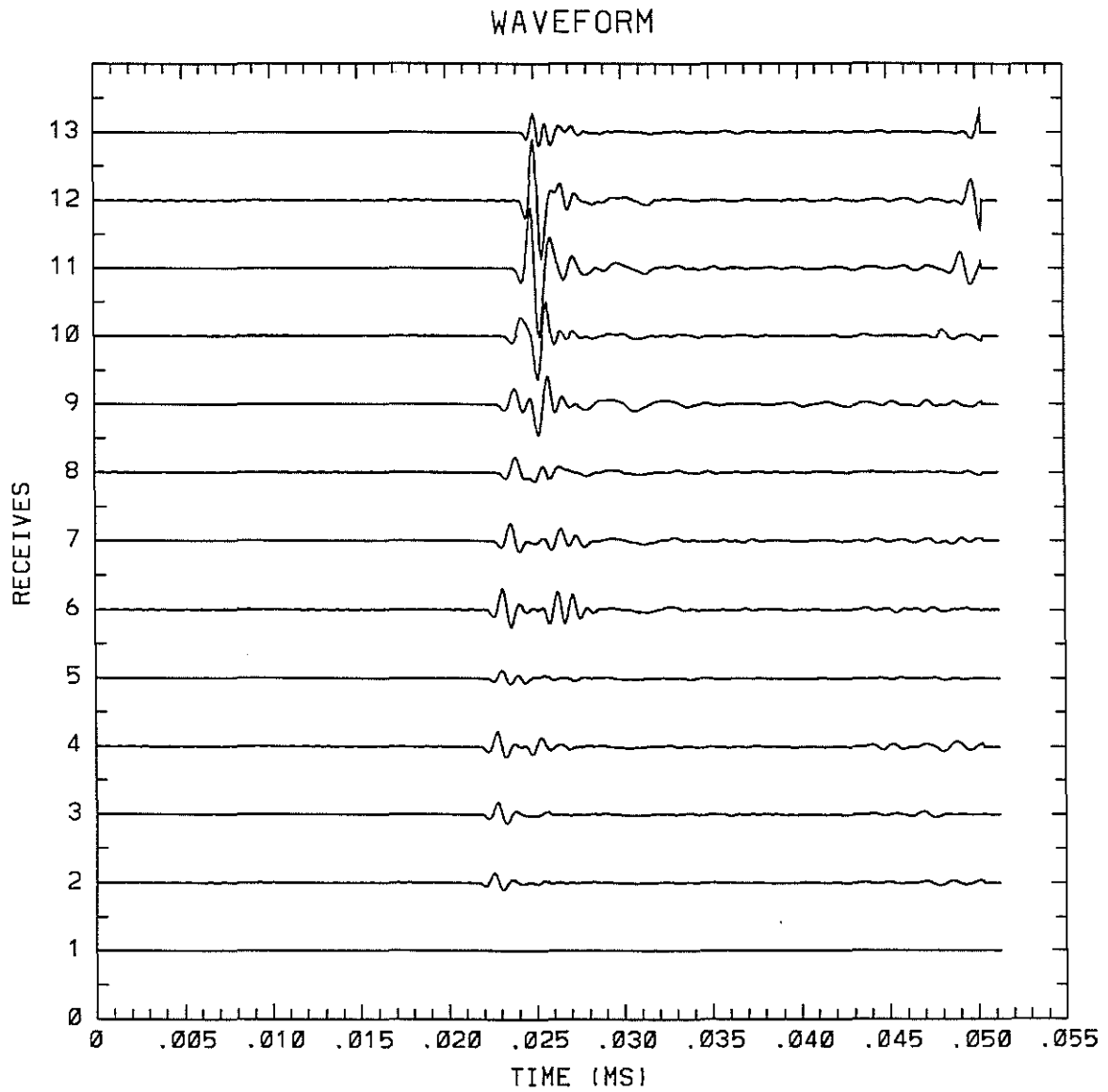
WAVEFORM

Figure A-4: Waveforms measured at various azimuthal directions from the source transducer (S source and P receiver).